

## Article

# Stability of the Photoluminescent Response on Hydroxyapatite/Multi-Walled Carbon Nanotube Composites

Edna X. Figueroa-Rosales <sup>1</sup>, Daniel Hernández-Cruz <sup>2</sup>, María J. Robles-Águila <sup>1</sup>,  
Mario E. Rodríguez-García <sup>3</sup> and Javier Martínez-Juárez <sup>1,\*</sup>

<sup>1</sup> Posgrado en Dispositivos Semiconductores, Instituto de Ciencias, Benemerita Universidad Autonoma de Puebla, Av. San Claudio y Boulevard 14 Sur, Ciudad Universitaria, Puebla 72570, Mexico; edna.figueroa@viep.com.mx (E.X.F.-R.); josefina.robles@correo.buap.mx (M.J.R.-Á.)

<sup>2</sup> Facultad de Ingenieria, Universidad Autonoma de Chiapas, Blvd. Belisario Dominguez, Km. 1081, Tuxtla Gutierrez 29050, Chiapas, Mexico; daniel.hernandez@unach.mx

<sup>3</sup> Departamento de Nanotecnologia, Centro de Fisica Aplicada y Tecnologia Avanzada, Universidad Nacional Autonoma de Mexico, Campus Juriquilla, Queretaro 76230, Mexico; marioga@fata.unam.mx

\* Correspondence: javier.martinez@viep.com.mx; Tel.: +52-222-229-5500 (ext. 7873)

**Abstract:** The application of hydroxyapatite (HAp)/multi-walled carbon nanotube composites in the medical area as coatings in prosthetics has been widely used because the carbon nanotubes reinforce the mechanical properties of hydroxyapatite. Despite that, their photoluminescent properties have not been studied, nor has the effect of different amounts of multi-walled carbon nanotubes on this property or what happened with their response with time. This work demonstrated that the photoluminescent response of HAp and HAp/multi-walled carbon nanotubes functionalized with oxygen groups (OMWCNT) composites was stabilized over time. The evaluated parameters were: three different amounts of OMWCNT (15, 25, and 35 mg) and two different thermal treatment temperatures (250 and 400 °C); all the samples were measured twice, after preparation and over a year after. The results indicated that over time the photoluminescent response is stabilized due to the passivation of surface defects, independently of the amount of OMWCNT used and the thermal treatment. In the end, the photoluminescent properties of these composites will extend their utilization in the medical area or open the door to new applications.



**Citation:** Figueroa-Rosales, E.X.; Hernández-Cruz, D.; Robles-Águila, M.J.; Rodríguez-García, M.E.; Martínez-Juárez, J. Stability of the Photoluminescent Response on Hydroxyapatite/Multi-Walled Carbon Nanotube Composites. *Photonics* **2023**, *10*, 919. <https://doi.org/10.3390/photonics10080919>

Received: 30 June 2023

Revised: 27 July 2023

Accepted: 31 July 2023

Published: 10 August 2023



**Copyright:** © 2023 by the authors. Licensee MDPI, Basel, Switzerland. This article is an open access article distributed under the terms and conditions of the Creative Commons Attribution (CC BY) license (<https://creativecommons.org/licenses/by/4.0/>).

**Keywords:** hydroxyapatite; multi-walled carbon nanotubes; photoluminescence; stabilization; composites

## 1. Introduction

Hydroxyapatite (HAp) and HAp/multi-walled carbon nanotube (MWCNT) composites are gaining interest due to their medical applications. HAp has been used in bone regeneration and drug delivery [1–6], and in the composites, their osteoblast cell response has been evaluated to use them as coatings [6,7]. This is because HAp is compatible with human bones and other tissues of the body [6]. Another of these medical applications for HAp is its use as a bioimaging agent. It has been modified with a series of ions that partially replace  $\text{Ca}^{2+}$ , such as  $\text{Fe}^{3+}$  [8] and  $\text{Mn}^{2+}$  [9], or the rare earths  $\text{Tb}^{3+}$ ,  $\text{La}^{3+}$ ,  $\text{Er}^{3+}$ ,  $\text{Dy}^{3+}$ ,  $\text{Eu}^{3+}$ , and  $\text{Gd}^{3+}$  [10,11]. Photoluminescent properties with medical applications are not often achieved because the used metals are toxic and have an aggregation-caused quenching (ACQ) effect on conventional fluorophores, which precludes their use [12–15]. To overcome these limitations, it is crucial to use non-toxic materials and eliminate the ACQ effect, as these properties are important for efficient light emission in this field. Some examples of the application of the photoluminescent properties of HAp are the experiments conducted by Yang et al. [16] and Chen et al. [17]. Yang et al. monitored the reduction in the intensity of photoluminescent mesoporous silica/apatite composites as a bioindicator of the release of captopril in simulated body fluid [16]. Chen et al. showed that  $\text{Eu}^{3+}/\text{Gd}^{3+}$ -HAp

nanorods can be used to obtain photoluminescence and computed tomography images [17]. In this way, carbon nanotubes (CNT) are promising materials because they have excellent biocompatibility, a large surface area, and structural, optical, thermal, electrical, and mechanical properties [7,18,19]. Moreover, previous studies have demonstrated the luminescent properties of single-walled carbon nanotubes (SWCNT) and MWCNT when they are dispersed [20,21].

Another recent application for HAp has been in the creation of a pc-LED, where Zhang et al. [22] found a highly intense blue photoluminescent response due to the incorporation of B into Ce<sup>3+</sup> doped-hydroxyapatite; at the same time, they assigned it to the reduction of OH<sup>-</sup> vibrations in the HAp lattice. Given that the vibrations of the OH<sup>-</sup> groups can decrease the photoluminescent efficiency or quench the emission at all [23]. Consequently, the generation of OH<sup>-</sup> vacancies in HAp is a good way to improve its photoluminescent properties. The enhancement of the photoluminescence due to defects (self-active photoluminescence) in the HAp has been investigated by Machado et al. [24]. They studied the effect of thermal treatment on the photoluminescent properties of HAp. As the temperature increases, the photoluminescent properties of HAp shift from the blue-green region (200–350 °C) to the yellow-orange region (400–550 °C) and then return to the blue-green region (600–800 °C). This was attributed mainly to OH<sup>-</sup> and H<sup>+</sup> vacancies, as well as surface, interface, and bulk defects due to the different thermal treatment temperatures. In this new use of HAp, CNT can be useful because they have been employed to make organic light-emitting diodes [25]. However, as reported by Fournet et al. [26], an adequate amount of CNT has to be found before the luminescent response decays because of the increased conduction of the material.

Until now, the shift in the maximum emission value of HAp has been reached with rare earth elements, transition metals, defects in the HAp structure, and currently with the help of functionalized oxygen groups MWCNT (OMWCNT) [27]. The background given by Zhang et al. [22], Machado et al. [24], and Figueroa-Rosales et al. [27] shows the opportunity to study the impact of defects and the amount of OMWCNT in the photoluminescent properties of HAp. On the other hand, the stabilization of the photoluminescent properties of HAp or HAp/MWCNT composites over time has not been reported.

In this work, it was exhibited that the photoluminescent response of HAp and HAp/OMWCNT composites was stabilized with time. HAp powders containing different amounts of OMWCNT (15, 25, and 35 mg) were incorporated and then thermally treated at 250 and 400 °C. Samples were measured after preparation and around one year later to study the stabilization of the photoluminescence emission.

## 2. Materials and Methods

Calcium nitrate tetrahydrate (Ca(NO<sub>3</sub>)<sub>2</sub>·4H<sub>2</sub>O, 100% Fermont), di-ammonium hydrogen phosphate ([NH<sub>4</sub>]<sub>2</sub>HPO<sub>4</sub>, 99.3% Fermont), Trizma base (C<sub>4</sub>H<sub>11</sub>NO<sub>3</sub>, >99.9% Sigma-Aldrich, St. Louis, MO, USA), and ammonium hydroxide (NH<sub>4</sub>OH, 28–30% Meyer, Mexico City, Mexico) were used as HAp precursors. Hexadecyltrimethylammonium (CTAB, 99% Sigma-Aldrich, St. Louis, MO, USA) was used as a surfactant.

### 2.1. Hydroxyapatite Synthesis

A solution of 0.1 M Trizma base was used to prepare the solutions of di-ammonium hydrogen phosphate and calcium nitrate. A solution of 0.37 M di-ammonium hydrogen phosphate ([NH<sub>4</sub>]<sub>2</sub>HPO<sub>4</sub>) was stirred at room temperature. Then, a 0.85 M solution of calcium nitrate tetrahydrate (Ca(NO<sub>3</sub>)<sub>2</sub>·4H<sub>2</sub>O) was slowly dropped into the phosphate solution. A solution of 0.2 M CTAB was added to the solution with constant stirring. The pH of the solution was adjusted to 10 ± 1 with ammonium hydroxide (NH<sub>4</sub>OH). After the precipitation, the mixture was sonicated in the Ultrasonic Processor (Sonics and Materials Inc., Newton, CT, USA) for 30 min at 70% amplitude and pulses of 2 s in active and inactive modes. The material was thoroughly washed with distilled water first, then with distilled water/ethanol (1:1) to remove the residual salts from the synthesis, aged for 24 h, and dried

at 100 °C for 5 h in a Sev model MF3 muffle. Finally, the sample was ground in an agate mortar and then subjected to a thermal treatment at 250 °C and 400 °C for 3 h (Sev model MF3) to obtain the HAp powder. Samples were called HAp250 and HAp400 for the two different thermal treatments, as can be seen in Figure 1.

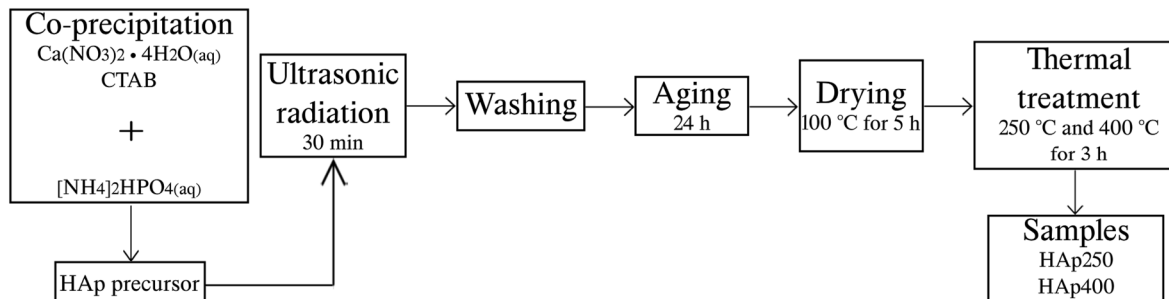


Figure 1. Chart flow of the synthesis of HAp250 and HAp400.

2.2. Hydroxyapatite/OMWCNT Composites Preparation

OMWCNT was used to prepare the composite samples. They were synthesized according to the CASTLE methodology [28].

In different flasks, 15, 25, and 35 mg (1.5, 2.5, and 3.5%) of nanotubes were dispersed in a 5% *v/v* Triton X100 solution for 1 h at  $65 \pm 5$  °C with constant stirring. Then, the three flasks were shaken in an ultrasonic bath (Cole-Parmer model 08895-04) for 1 h at the same temperature. After that, 1 g of HAp precursors (without thermal treatment) was added to each dispersion, and the samples were subjected to the same process as OMWCNT. After 18 h of resting, each sample was washed by microfiltration with distilled water and ethanol separately and then thermally treated at 250 °C and 400 °C for 3 h, respectively. The final samples were designated HAp250 or HAp400 along with the amount of OMWCNT used in them; for example, a composite with 15 mg of OMWCNT and thermal treatment at 250 °C is named HAp250-15, and so on. Figure 2 shows the composite preparations and how they were named.

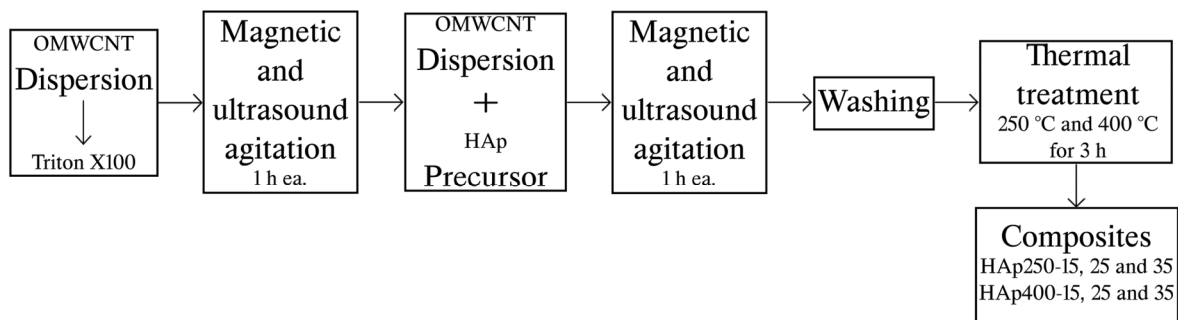


Figure 2. Diagram of the composite preparation at 250 and 400 °C and three different amounts of OMWCNT (15, 25, and 35 mg).

2.3. Characterization

To identify the crystalline structure of the materials, X-ray powder diffraction (XRD) patterns were collected on a Bruker diffractometer (Discovery D8) operating at 40 kV and 40 mA in horizontal configuration  $\theta$ - $2\theta$ , the geometry of parallel beam with a Göbel mirror, and a point type scintillation detector. The measurements were carried out with the following settings: from 5–80° at  $\lambda = 1.5406$  Å for 4 h, with a 0.02° step and a counting time of 3.84 s. The crystallite size was calculated by the modified Scherrer equation (Monshi-Scherrer Method) as follows:  $\text{Ln}\beta = \text{Ln}\left(\frac{\text{K}\lambda}{L}\right) + \text{Ln}\left(\frac{1}{\cos\theta}\right)$  [29]. It was graphed  $\text{Ln}\beta$  vs.  $\text{Ln}\left(\frac{1}{\cos\theta}\right)$  and by the operation  $e^{\text{Ln}\frac{\text{K}\lambda}{L}} = \frac{0.89 \times 0.15405}{L}$ , the crystallite size was obtained in

each sample. The morphology of HAp and OMWCNT was determined using a high vacuum Hitachi (SU8230) scanning electron microscope, with a resolution of  $50,000\times$  and  $100,000\times$  at 1.0 kV electron acceleration voltage. The samples were fixed in a copper sample holder with carbon tape and covered with a thin gold film to make them conductive before testing. Additionally, HAp250 was measured with a resolution of  $100,000\times$  and  $200,000\times$  at 30.0 kV electron acceleration voltage in Scanning Transmission (STEM) and Bright Field Scanning Transmission Electron Microscopy (BF-STEM), respectively. The sample was dispersed in ethanol, and then a drop was dried in a grid holder. The FTIR spectroscopy measurements were performed on a Nicolet 6700 spectrophotometer (Thermo Scientific, Waltham, MA, USA) equipped with an ATR (Attenuated Total Reflectance) accessory Smart iTR (Thermo Scientific) with a diamond crystal, in the spectral interval of  $4000\text{--}650\text{ cm}^{-1}$  with a spectral resolution of  $4\text{ cm}^{-1}$ . To analyze the excitonic states in the HAp and its composites, photoluminescent (PL) experiments were conducted on a homemade spectrofluorometer with two different detectors. The first one was a Si PIN detector and the second one was a photomultiplier tube from Hamamatsu (R636-10); the last was used to measure the composites at  $400\text{ }^\circ\text{C}$  on the second measurement, due to the low signal from them. The materials were excited with a He-Cd laser at 325 nm and analyzed at 350–800 nm. To evaluate the samples, a small amount of powder was compressed in a disc shape at  $1\text{ ton/cm}^2$  using a hydraulic press (SpectroPress, Chemplex, Industries, Inc., Palm City, FL, USA).

### 3. Results and Discussion

#### 3.1. X-ray Diffraction

Figure 3a–h shows the X-ray diffraction patterns of all the samples; even when the composites had different amounts of OMWCNT, the patterns did not display any peak related to it because their peaks overlapped with the ones for HAp at (002), (100), and (004) reflections. According to Arul & Vijayalakshmi [30], the peaks of OMWCNT become evident with 4% of them in the sample; in this case, the maximum concentration used was 3.5%. Thus, all the prepared samples were identified as hydroxyapatite with a hexagonal crystalline structure, which was determined using the 00-009-0432 card PDF+-4 database ICDD [31]. Other calcium phosphates, such as  $\alpha$  or  $\beta$  tricalcium phosphate, were not located in the patterns because the synthesis method did not favor their formation and the thermal treatment temperatures used were below the ones at which these phases crystallize (above  $700\text{ }^\circ\text{C}$ ) [32]. These X-ray patterns exhibited broad peaks that, according to Londoño-Restrepo et al. [33], are related to the simultaneous elastic and inelastic X-ray scattering due to the HAp nanocrystalline size. This was correlated when calculating the crystallite size using the Monshi–Scherrer method [29] on the peaks at (002), (112), (202), (212), (310), and (221). The effect of thermal treatment on HAp250 and HAp400 did not significantly affect the crystallite size. Nevertheless, the addition of OMWCNT in the composites increased, decreased, and increased again the crystallite size while the amount of OMWCNT increased, as can be seen in Table 1. Though comparing the crystallite size of the three amounts of OMWCNT at the two different thermal treatment temperatures, the crystallite size of the samples at  $400\text{ }^\circ\text{C}$  was slightly smaller than the ones at  $250\text{ }^\circ\text{C}$ . According to our previous work [27], the addition of OMWCNT increased the crystallite size; however, their aggregation in the composites occurred during the coprecipitation process, and the exposure time to thermal treatment was longer (6 h) than now (3 h). In this work, the OMWCNT were added after the HAp powders were obtained. This means that the OMWCNT did not improve the crystallinity of the HAp because it had already been synthesized. Nevertheless, their presence influenced the impact of the thermal treatment even when the behavior was increased, decreased, and increased again. It is worth noting that just the minimum amount of OMWCNT helped to increase the crystallite size. The other two amounts of them reduced this value because they messed up with the growth of HAp by means of the thermal treatment, in both batches.

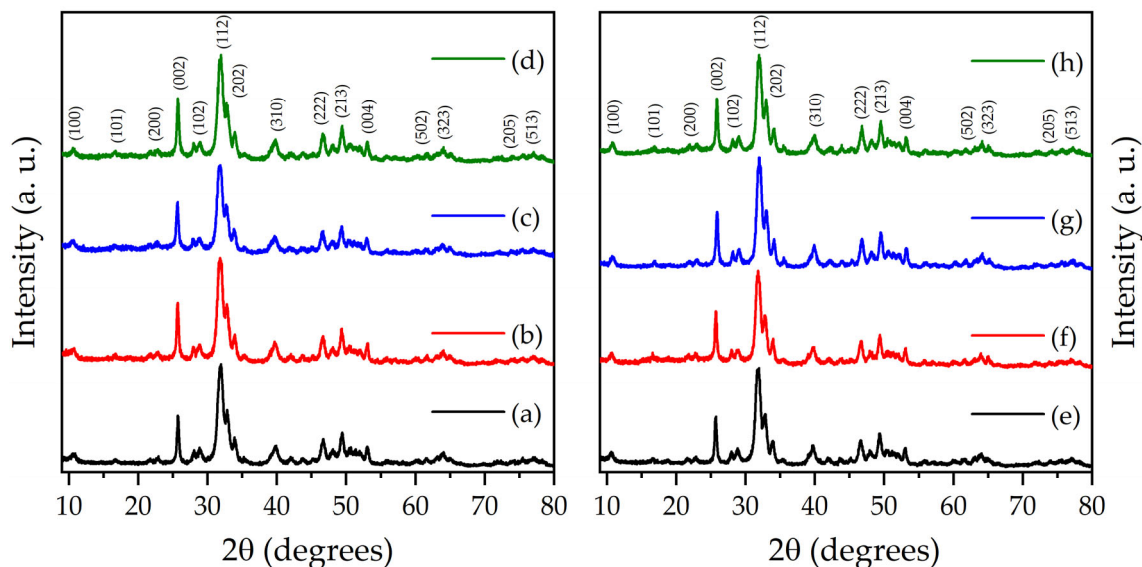


**Figure 3.** X-ray diffraction patterns of (a) HAp250, (b) HAp250-15, (c) HAp250-25, (d) HAp250-35, (e) HAp400, (f) HAp400-15, (g) HAp400-25, and (h) HAp400-35.

**Table 1.** Crystallite size of all the prepared samples calculated by Monshi–Scherrer method.

Sample	$e^{Ln \frac{K\lambda}{L}} = \frac{0.89 \times 0.15405}{L}$	Crystallite Size (nm)
HAp250	$e^{-5.70559} = 3.32 \times 10^{-3}$	41.2
HAp250-15	$e^{-5.88745} = 2.77 \times 10^{-3}$	49.4
HAp250-25	$e^{-5.42563} = 4.40 \times 10^{-3}$	31.1
HAp250-35	$e^{-5.66272} = 3.47 \times 10^{-3}$	39.5
HAp400	$e^{-5.65608} = 3.49 \times 10^{-3}$	39.2
HAp400-15	$e^{-5.8206} = 2.96 \times 10^{-3}$	46.2
HAp400-25	$e^{-5.42989} = 4.38 \times 10^{-3}$	31.3
HAp400-35	$e^{-5.65509} = 3.49 \times 10^{-3}$	39.2

### 3.2. SEM Analysis

The morphology of the samples and the presence of OMWCNT on the composites are shown in Figure 4a–h. All the samples are formed of irregular aggregates of HAp. However, as can be seen in Figure 5a,b, those aggregates are constructed of cylindrical particles, like bars, with dimensions around 38 nm. This way of growing was attributed to the presence of CTAB during the synthesis process due to the fact that this reactive forms a tetrahedral cation that interacts with the tetrahedral group of  $PO_4^{3-}$  ions [34]. In the case of the composites, the HAp aggregates can be on the OMWCNT or around them. Using the software ImageJ 1.54d, the thickness of the OMWCNT was measured in Figure 4, and for all the composites, the thickness of them was variable. Finding values from 14–100 nm means that the OMWCNT have suffered some kind of damage because their size is not uniform.

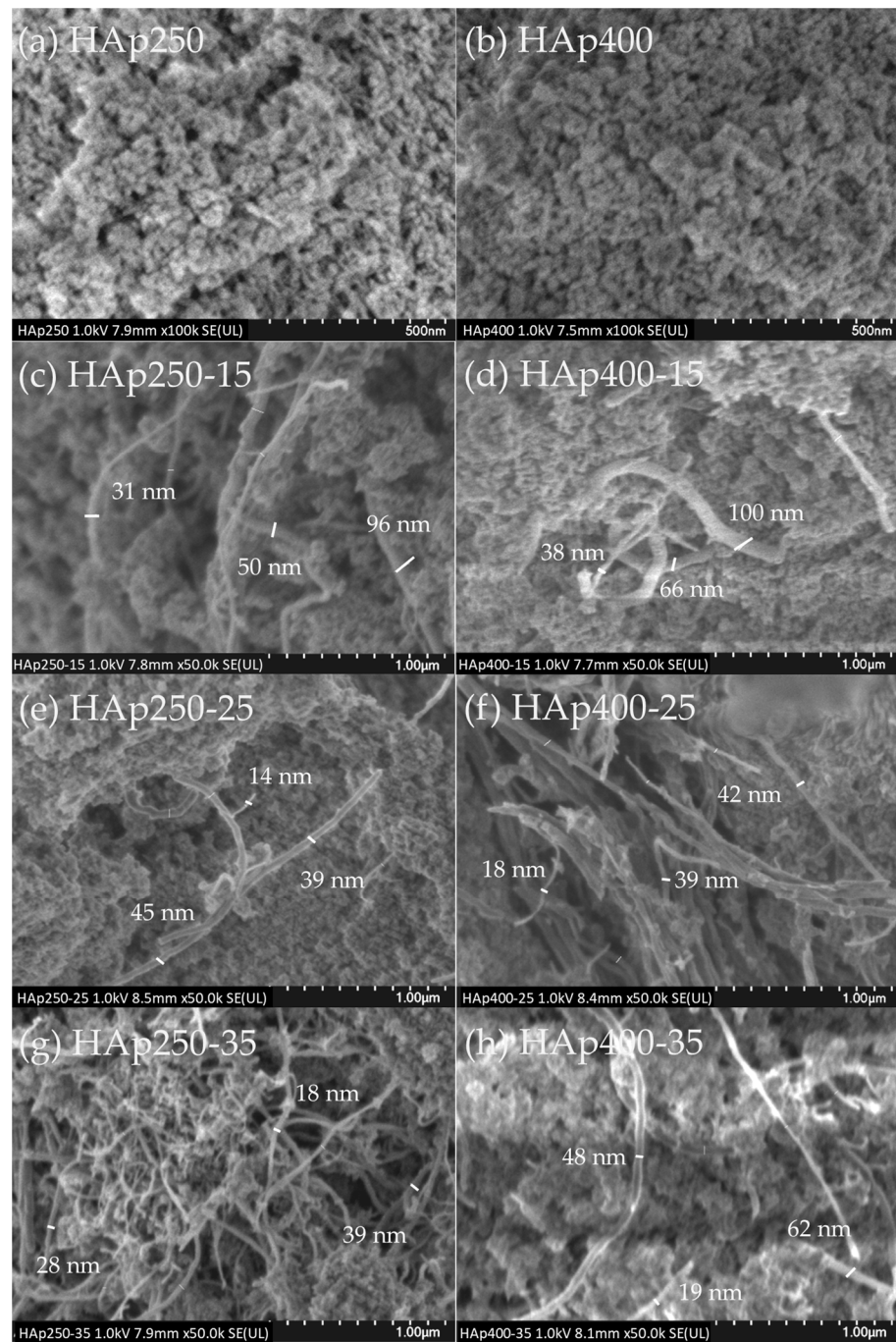


**Figure 4.** Scanning Electron Microscopy (SEM) images of (a) HAp250 and (b) HAp400 at 100,000 $\times$ ; (c) HAp250-15, (d) HAp400-15, (e) HAp250-25, (f) HAp400-25, (g) HAp250-35, and (h) HAp400-35 taken at 50,000 $\times$ .

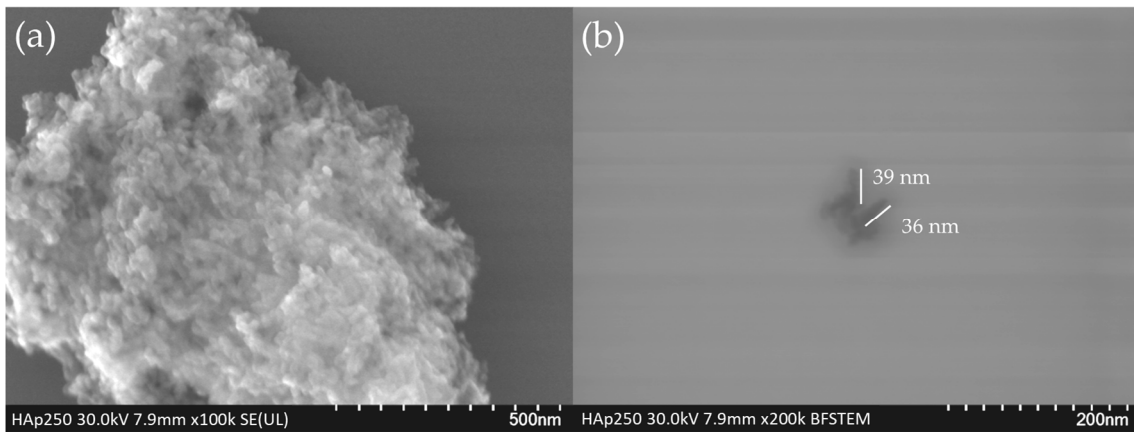


**Figure 5.** Micrographs of HAp250 in (a) Scanning Transmission Electron Microscopy (STEM) and (b) Bright Field Scanning Transmission Electron Microscopy (BF-STEM) modes.

### 3.3. FTIR Analysis

Figure 6a,b show four spectra of the samples on the first and second measurements; as was expected, every sample presented the characteristic vibrational states of HAp with slight differences (Table 2). Additionally, in the second measurement, vibrations corresponding to P-OH, O-H, and CO<sub>2</sub> were found. The bands shown between 2400–2250 cm<sup>-1</sup> were related to CO<sub>2</sub> present in the atmosphere when the measurement took place [35], but it was not adsorbed at all in the samples. On the other hand, the characteristic vibrational states of OMWCNT were not found because, as reported by Arul & Vijayalakshmi [30], the bands belonging to them appear above 4% of OMWCNT in the composite.

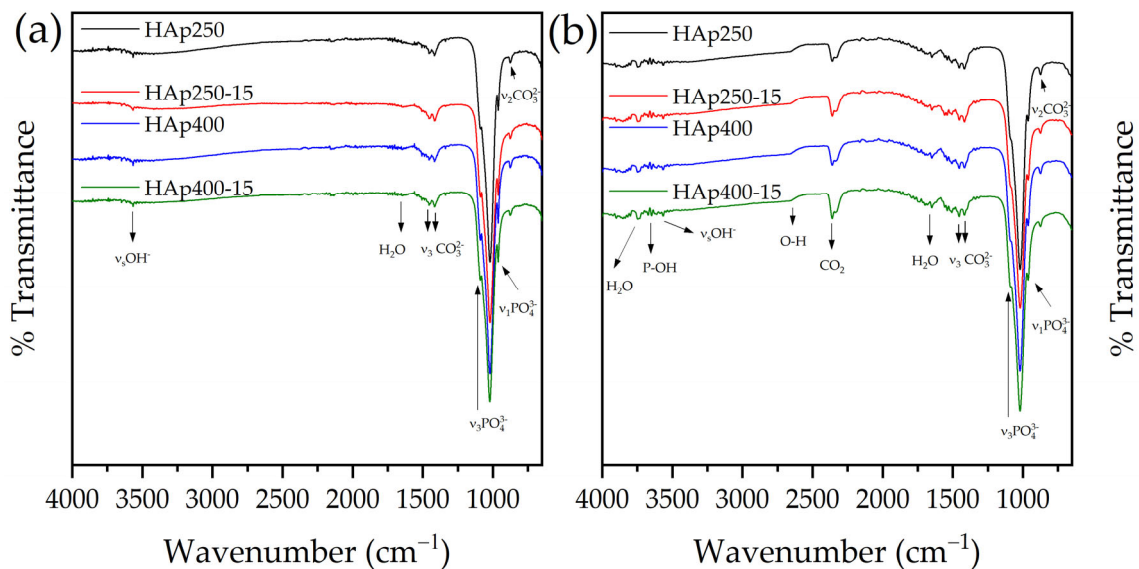


**Figure 6.** Fourier Transform Infrared (FTIR) spectra of HAp250, HAp250-15, HAp400, and HAp400-15 (a) at the first and (b) second measure.

To analyze the changes in the samples, the FWHM of some vibrational states was calculated. It was found that the FWHM at 3570 cm<sup>-1</sup> belonging to the OH stretching increased since the first measurement from 5–6 cm<sup>-1</sup> (FWHM at the first measure) to 15–19 cm<sup>-1</sup> (FWHM at the second measure), and it was greater for the batch at 400 °C than the one at 250 °C. This means that some of the dangling bonds on the surface of the samples had been neutralized over time and became bulk states. Since the samples were not stored in a controlled environment or a vacuum, the entrapment of CO<sub>2</sub> from the atmosphere occurred on the surface of every sample, stabilizing the superficial charges on

them by the following reaction,  $2\text{OH}^- + \text{CO}_2 \rightarrow \text{CO}_3^{2-} + \text{H}_2\text{O}$ , from which the  $3740\text{ cm}^{-1}$  band belonging to adsorbed water was generated. Then, those water molecules interact with the hydroxyl and phosphate ions on the surface of HAp. The weak bands between  $3680\text{--}3640\text{ cm}^{-1}$  belonging to P-OH groups supported this neutralization theory. Since it has been reported by Bertinetti et al. [36], the P-OH groups may constitute surface acidic phosphate ions,  $\text{HPO}_4^{2-}$ , in order to compensate for the overall charge balance in calcium-deficient HAp. Although the presence of the band belonging to  $\text{HPO}_4^{2-}$  ions was not observed in the FTIR spectra of any sample, as this phenomenon just happens on the surface of the materials. Another band that resulted from the vibration of the P-OH bond is the one between  $2750\text{--}2650\text{ cm}^{-1}$  relative in the literature to O-D vibrations because of the adsorption/desorption of H and D on the surface [36]. However, in the present work, no reactive containing D was used; in that case, the band corresponds to O-H vibrations.

**Table 2.** Characteristic vibrational states present in all the samples at the first and second measurements.

Band Position ( $\text{cm}^{-1}$ )		Assignment	Ref.
First Measurement	Second Measurement		
---	3740	Adsorbed water	[36]
---	3680–3640	P-OH vibration	[36,37]
3566	3566	O–H stretching	[37,38]
---	2750–2650	O-H vibration	[36]
---	2400–2250	$\text{CO}_2$ free	[35]
$1650 \pm 10$	$1660 \pm 10$	Adsorbed water and unstable $\text{CO}_2$ specie	[37,38]
1454	1457	$\text{CO}_3^{2-}$ replacing $\text{PO}_4^{3-}$	[37,38]
1413	1414	$\text{CO}_3^{2-}$ replacing $\text{OH}^-$	[37,38]
1094	1094	$\nu_3 \text{PO}_4^{3-}$	[37,38]
1021	1021	$\nu_3 \text{PO}_4^{3-}$	[37,38]
962	961	$\nu_1 \text{PO}_4^{3-}$	[37,38]
877	875	$\text{CO}_3^{2-}$ substitutions type A and B	[37,38]

The next deconvoluted band was the one around  $1650\text{ cm}^{-1}$  belonging to physisorbed water and an unstable  $\text{CO}_2$  species. Over time, the FWHM of every sample decreased and was shifted to higher wavenumbers, meaning that some  $\text{CO}_2$  was desorbed and it created  $\text{H}_2\text{O}$  ( $3740\text{ cm}^{-1}$  band) and  $\text{CO}_3^{2-}$  [36,37]. As an example, this region was deconvoluted for sample HAp250-15 at the first and second measurements, and it is presented in Figure 7a.

The correlated results came from the band referring to  $\text{CO}_3^{2-}$  ion replacements; this band was deconvoluted to three sub-bands at the first measurement and four bands at the second measurement, except for HAp250, which was deconvoluted to four bands at both measurements. The first two bands were assigned in Table 2, the third one at  $\sim 1496\text{ cm}^{-1}$  was referred to as  $\text{CO}_3^{2-}$  replacing  $\text{OH}^-$  (A site), and finally, the fourth one at  $1549 \pm 6\text{ cm}^{-1}$  was related to  $\text{CO}_3^{2-}$  replacing  $\text{PO}_4^{3-}$  (B site) [37]. The FWHM of the first band increased for the composites, which means that more  $\text{CO}_3^{2-}$  ions are in  $\text{OH}^-$  sites. In other words, the number of  $\text{OH}^-$  ion vacancies increased. For HAp250 and HAp400, it slightly decreased. On the contrary, the FWHM of the second band did not change for the composites, but it increased for HAp250 and HAp400, which means that more  $\text{CO}_3^{2-}$  ions are in  $\text{PO}_4^{3-}$  sites. The third band diminished for all the samples. Finally, the band at  $1549 \pm 6\text{ cm}^{-1}$  appeared for all the samples and decreased for HAp250; this band was assigned to substitution type B and to surface  $\text{CO}_3^{2-}$ . All these alterations can be explained by the fact that HAp is able to absorb  $\text{CO}_2$  from the atmosphere, which was detected at the first measurement around  $1650\text{ cm}^{-1}$ . By the reaction mentioned above, it reacts

with surface  $\text{OH}^-$  ions, and  $\text{CO}_3^{2-}$  ions take their site [37],  $2\text{OH}^- + \text{CO}_2 \rightarrow \text{CO}_3^{2-} + \text{H}_2\text{O}$ , which is according to the aforementioned for band one where the A-type substitutions were enhanced. It also explained the creation of the fourth band in the samples where not all the  $\text{CO}_3^{2-}$  ions have been incorporated in the lattice, as can be seen in the comparison of Figure 7a for HAp250-15 at the first and second measurements.

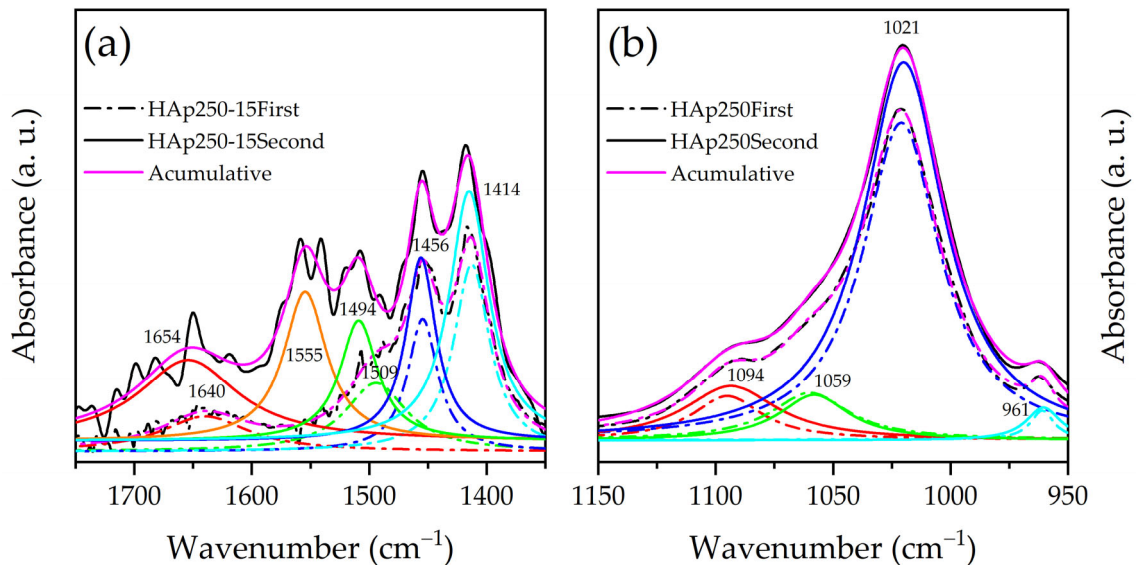


**Figure 7.** Deconvolution of the  $\text{CO}_3^{2-}$  and  $\text{PO}_4^{3-}$  bands for samples (a) HAp250-15 and (b) HAp250, respectively, at the first and second measurements.

The band belonging to the  $\nu_3 \text{PO}_4^{3-}$  vibrational state was deconvoluted into three sub-bands [39]. Figure 7b shows the deconvolution of this band for HAp250 at the first and second measurements. The middle band at  $\sim 1059 \text{ cm}^{-1}$  is not listed in Table 2. The FWHM of the band at  $1021 \text{ cm}^{-1}$  did not change over time, but the other two did; one diminished and the other increased for all the samples. In other words, the surface dangling bonds of the  $\text{PO}_4^{3-}$  group became bulk states. The FWHM at  $\sim 961 \text{ cm}^{-1}$  belonging to the symmetric stretching vibration of the  $\text{PO}_4^{3-}$  group increased for all the samples too.

At last, the band at  $875 \text{ cm}^{-1}$  was deconvoluted into two sub-bands at  $872$  and  $878 \text{ cm}^{-1}$ . According to the literature, the ratio of the intensities of the bands at  $880$  and  $872 \text{ cm}^{-1}$  gives the ratio of the A-type-to-B-type carbonated apatite [38]. In the case of HAp250, the ratio was maintained (Figure 8a), and for HAp400, this ratio increased, as can be seen in Figure 8b. In the other samples, the ratio slightly decreased from the original value, which means that the amount of  $\text{CO}_3^{2-}$  ions in  $\text{PO}_4^{3-}$  sites increased. All these changes are reflected in their photoluminescent properties.

### 3.4. Photoluminescence Analysis

Figure 9a–d presents the photoluminescence spectra of HAp250 and HAp400 in the first and second measurements. The first measurement of HAp250 (Figure 9a) showed a maximum emission band at  $490 \text{ nm}$  and the second one at  $503 \text{ nm}$  (Figure 9c); in addition to this change, the intensity of the emission increased around three times since the original measurement, being that HAp is not photoluminescent for itself [40]. The cause of this phenomenon is defects in the HAp lattice, created during the synthesis process and after it because of the entrapment of  $\text{CO}_2$  from the atmosphere due to the samples were not stored in a vacuum. In Table 3, the defects related to every deconvoluted band shown in Figure 9 are listed. For both spectra, HAp250's first and second measurements are attributed to oxygen vacancies from  $\text{OH}^-$  and  $\text{PO}_4^{3-}$  ions and  $\text{OH}^-$  and  $\text{Ca}^{2+}$  ion vacancies [41,42]. Even when the defects are the same for both measurements, the shift and the increase in intensity can be explained by the FTIR results. Where the B-type substitution of  $\text{CO}_3^{2-}$  was favored,

in other words, there was an increment in the  $\text{PO}_4^{3-}$  ion vacancies. This is in accordance with the increment in the intensity of the band at 551 nm in the photoluminescent spectra of Figure 9c. On the other hand, the increased intensity of the first two bands can be related to the presence of H. It has been reported that the energy linked to the presence of interstitial H appears in the forbidden zone near the valence band [43]. Even when there was not directly a band for this contribution, the FTIR results showed the presence of H in the samples, which suggests that the said band is overlapped because of the great intensity of the 434 nm and 491 nm bands.

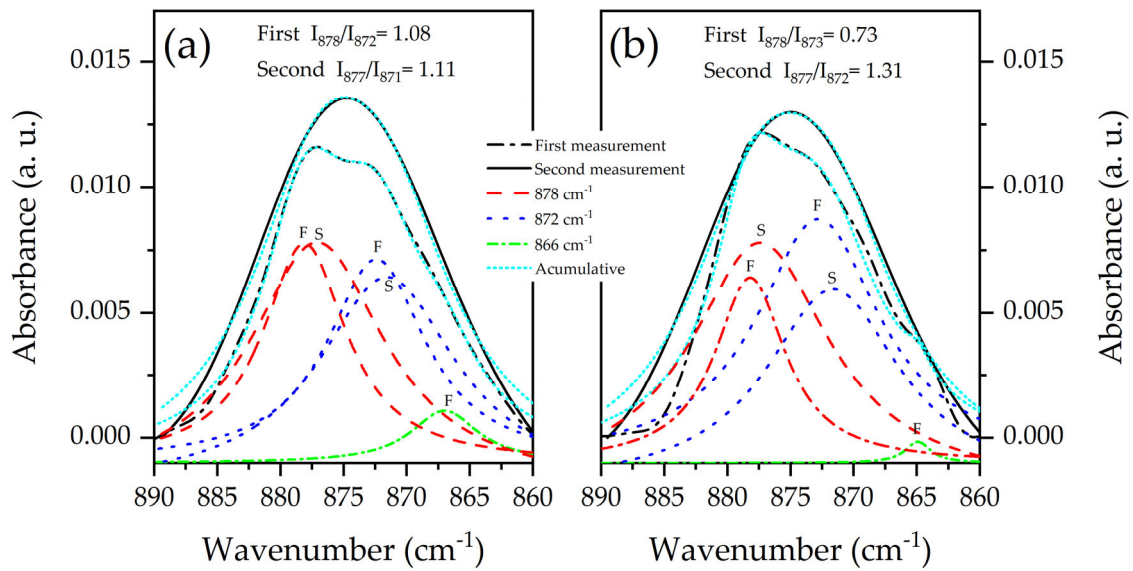


**Figure 8.** Deconvolution of the band at  $875\text{ cm}^{-1}$  for samples (a) HAp250 and (b) HAp400, respectively, at the first and second measurements.

**Table 3.** Assignment of the deconvoluted bands of Figure 9 for HAp250 and HAp400, at the first and second measures.

Measure	Sample	Band	Wavelength (nm)	Associate to	Ref.
First	HAp250	1	435	Oxygen vacancies from $\text{OH}^-$ ion and $\text{OH}^-$ ion vacancies	[41,42]
		2	483	$\text{OH}^-$ and $\text{Ca}^{2+}$ ion vacancies	[41,42]
		3	551	Oxygen vacancies from $\text{PO}_4^{3-}$ ion	[41,42]
	HAp400	3	562	Oxygen vacancies from $\text{PO}_4^{3-}$ ion	[41,42]
		I	653	$\text{OH}^-$ ion vacancies	[41,42]
Second	HAp250	1	434	Oxygen vacancies from $\text{OH}^-$ ion and $\text{OH}^-$ ion vacancies	[41,42]
		2	491	$\text{OH}^-$ and $\text{Ca}^{2+}$ ion vacancies	[41,42]
		3	551	Oxygen vacancies from $\text{PO}_4^{3-}$ ion	[41,42]
	HAp400	1	440	Oxygen vacancies from $\text{OH}^-$ ion and $\text{OH}^-$ ion vacancies	[41,42]
		2	494	$\text{OH}^-$ and $\text{Ca}^{2+}$ ion vacancies	[41,42]
		3	545	Oxygen vacancies from $\text{PO}_4^{3-}$ ion	[41,42]
		$\alpha$	615	Oxygen vacancies from $\text{PO}_4^{3-}$ ion	[41,42]

For the sample HAp400, the first measurement displayed a maximum emission band at 574 nm (Figure 9b) and the second one at 520 nm (Figure 9d). As with HAp250, HAp400 presented an increment in intensity, in this case about two times greater than the original measurement. At the first measurement, the photoluminescent emission was attributed to oxygen vacancies from  $\text{PO}_4^{3-}$  ions and  $\text{OH}^-$  ion vacancies [41,42]. In contrast, at the second measurement, the emission of the sample was referred to as oxygen vacancies from

$\text{OH}^-$  and  $\text{PO}_4^{3-}$  ions and  $\text{OH}^-$  and  $\text{Ca}^{2+}$  ion vacancies [41,42]. These modifications can be explained by the FTIR results too, where the substitution A-type was favored at the second measurement of the sample (Figure 8b), and then the bands at 440 and 494 nm appeared.

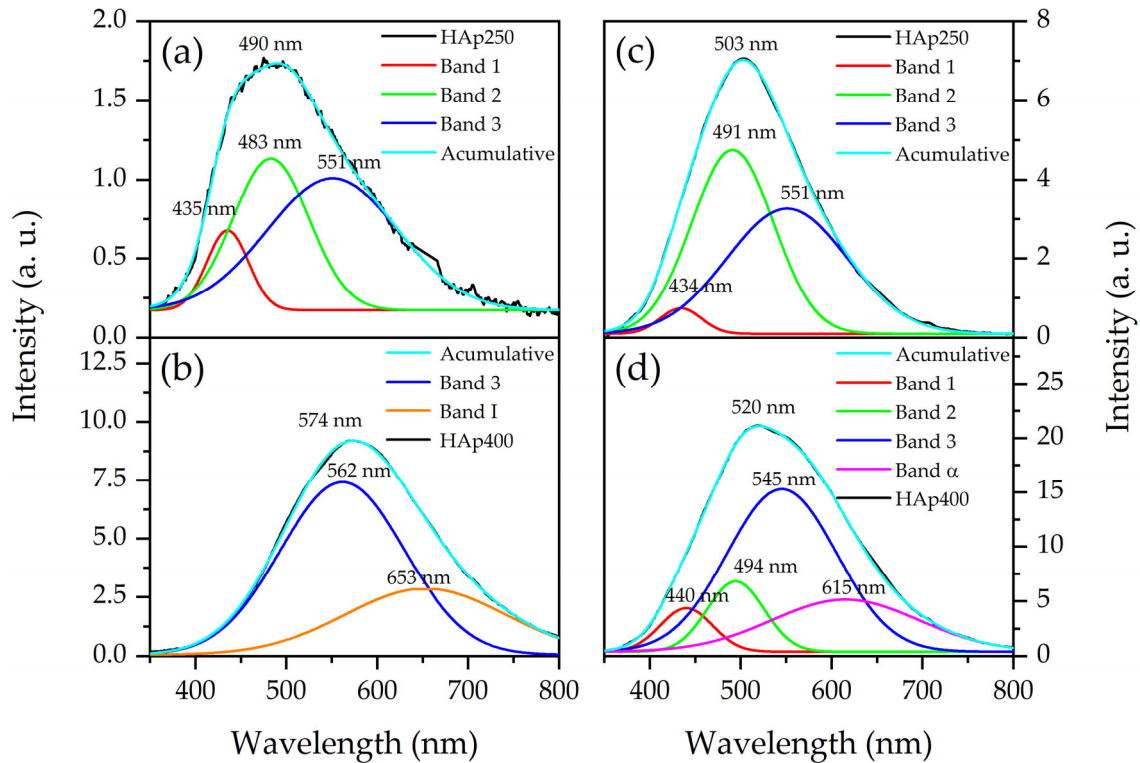


**Figure 9.** Photoluminescence spectra of HAp250 and HAp400 (a,b) at first and (c,d) at the second measures.

Both results at the first measurement are in agreement with those of Machado et al. [24], who investigated the effect of thermal treatment on the photoluminescent properties of HAp at 200–800 °C. However, the final results of the HAp25a and HAp400, which both reached the same photoluminescent emission range after some time have not been reported. Nevertheless, it proves that HAp exposed to ambient conditions attained stable photoluminescent emission over time in the blue-green region.

Comparing the results of each sample in the original and the second measurement, the intensities differed by a factor of four between HAp250 Figure 9a,c. In the case of HAp400, Figure 9b,d the gap was about two times. Following the work of Machado et al. [24], they attributed the photoluminescence response to surface, interface, and bulk defects due to the increase in heat treatment temperature and, at the same time, to the improvement of the crystallinity. In this work, according to the results of FTIR analysis, the surface defects in HAp250 and HAp400 became part of the bulk states present in each sample with time. In other words, what Machado et al. [24] achieved with thermal treatment was obtained here and stabilized over time. Due to this phenomenon, the maximum emission of HAp400 shifted to the blue-green region, and in both samples (HAp250 and HAp400), the intensity increased, indicating that the defects responsible for the photoluminescence of the sample are located within the lattice and not at the surface. For HAp, several computational studies were performed to understand how different types of defects in the HAp lattice produce energy labels within the forbidden band gap [41,43,44]. As can be seen in Table 3, the defects responsible for photoluminescence in HAp250 and HAp400 one year after reaching equilibrium were the same defects as in HAp250 one year earlier. This means that the most stable defects in hydroxyapatite are oxygen vacancies of  $\text{OH}^-$  and  $\text{PO}_4^{3-}$  ions and  $\text{OH}^-$

and Ca<sup>2+</sup> ion vacancies [41,42], which are formed at low thermal treatment temperatures. According to Machado et al. [24], the range is from 80–300 °C.

With the addition of carbon nanotubes, the maximum emission of HAp changed, as shown in Figure 10a–d. The first differences in Figure 10a,b are the decreasing intensity and the shift of the maximum emission band to higher wavelengths, with the amount of OMWCNT increasing. This shift happened due to the maximum emission of OMWCNT being at 610 nm [45], and the combination of both emissions (HAp and OMWCNT) gave an intermedium response in the composites. HAp400-35 was the exception in terms of redshift, but it was in the same yellow-orange interval as its batch. The decreased intensity in the samples can be explained because of the agglomeration [20] and the adsorption/desorption of CO<sub>2</sub> on the surface of the OMWCNT, which leads to the unzipping of their external sheets [46]. In the second measurement, the composites still showed lower intensity than their reference HAp (Figure 10c,d), but the measurements at 400 °C had almost disappeared because, in their case, a Hamamatsu photomultiplier tube (R636-10) was used to obtain the spectra. These results are attributed to the unzipping of the OMWCNT [46] because of the adsorption/desorption of CO<sub>2</sub> that was explained in the FTIR section and to the increased OH<sup>-</sup> vibrations. In addition, different thicknesses of the OMWCNT can be seen in Figure 4d,f,h. For this reason, the measurements at 400 °C will not be discussed further. Focusing attention on the composites at 250 °C at the second measurement, the maximum emission from each sample reached equilibrium around 518 nm. The varying amounts of OMWCNTs helped to maintain the red shift on the composites, with an average displacement of 16 nm from the initial measurement.

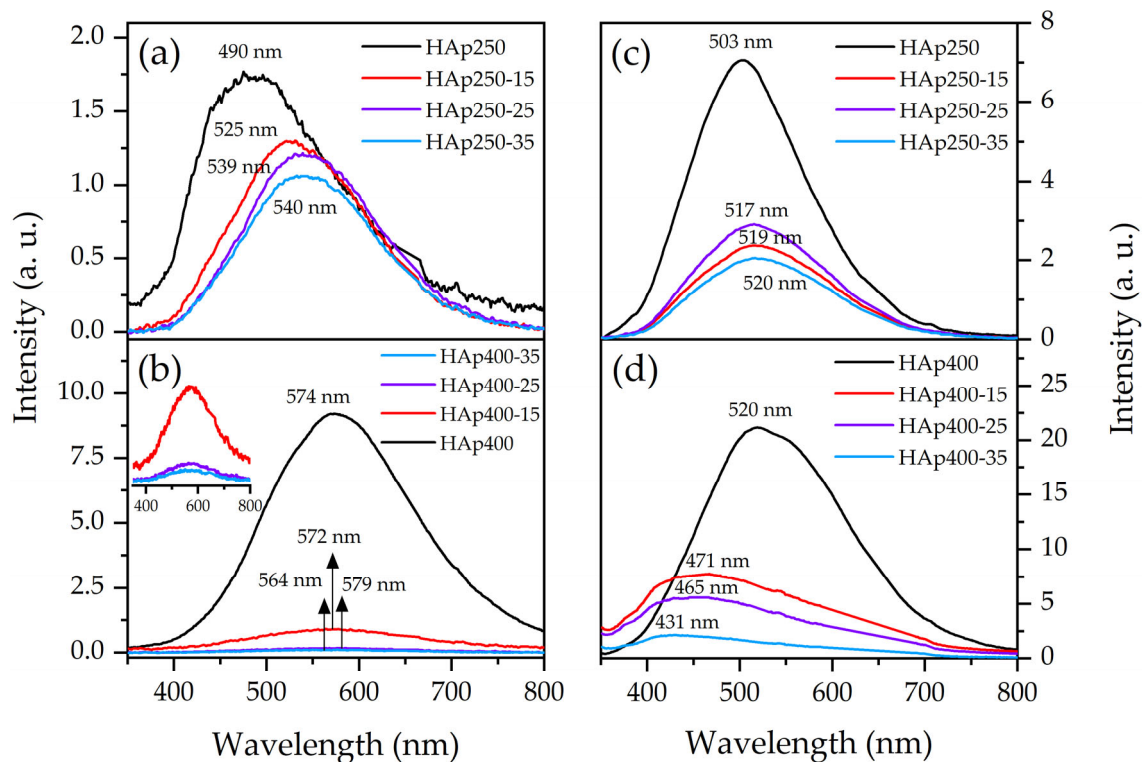


**Figure 10.** Photoluminescent spectra of all the samples (a,b) at the first and (c,d) at the second measures.

Similar to HAp250, the predominant defects responsible for the blue photoluminescence of the 250 °C composites are oxygen vacancies from OH<sup>-</sup> and PO<sub>4</sub><sup>3-</sup> ions and OH<sup>-</sup> and Ca<sup>2+</sup> ion vacancies [41,42]. Figure 11a,b shows the deconvolution of composite HAp250-15 in the first and second measurements, respectively. And Table 4 shows the assignment of each deconvoluted curve for the three composites. As can be seen from the

FTIR results, the surface defects contributed to the initial photoluminescent response of the sample, but over time these defects became part of the bulk states. The comparison between the first and second measures of HAp250-15 proved that the number of oxygen vacancies from OH<sup>-</sup> and PO<sub>4</sub><sup>3-</sup> ion increased, which is related to the entrapment of CO<sub>2</sub> from the atmosphere [37]. The contribution of OMWCNT at the second measurement was outshined by the oxygen vacancies from OH<sup>-</sup> and PO<sub>4</sub><sup>3-</sup> ions. In our previous work, the contribution of OMWCNT was not outshined because there was an interaction between them through a C=O bond [27]. Here, according to the FTIR results, there is no strong interaction between the HAp and OMWCNT because of the preparation of the composites by themselves.

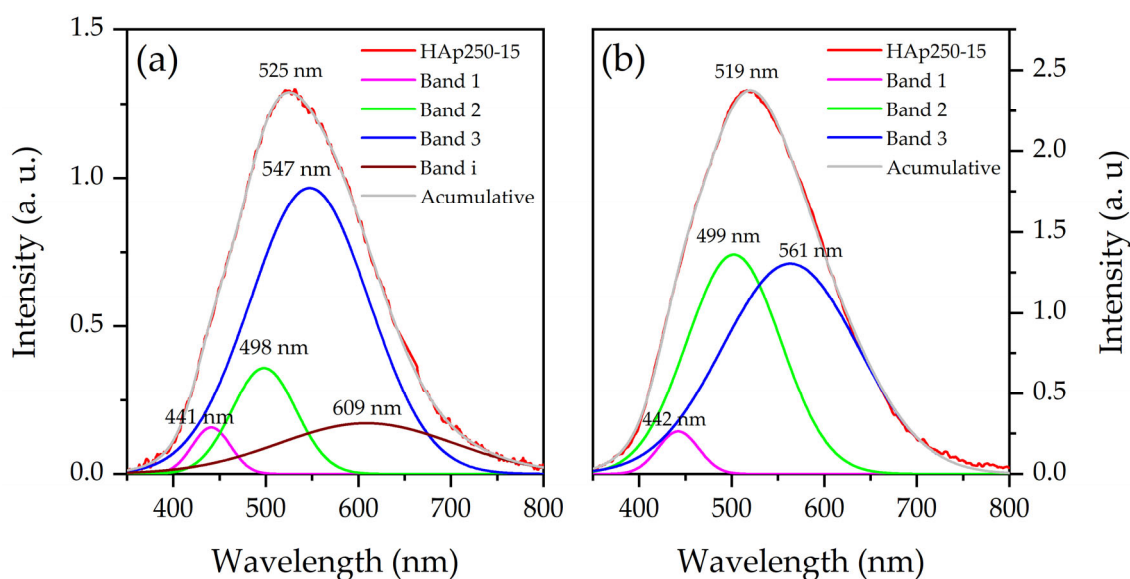


**Figure 11.** Deconvoluted photoluminescent spectra of HAp250-15 (a) at the first and (b) second measures.

**Table 4.** Assignment of the deconvoluted bands for the 250 °C composites at the first and second measures.

Measure	Sample	Band	Wavelength (nm)	Associate with	Ref.
First	HAp250-15 HAp250-25 HAp250-35	1	443 ± 1	Oxygen vacancies from OH <sup>-</sup> ion and OH <sup>-</sup> ion vacancies	[41,42]
		2	499 ± 2	Oxygen vacancies from OH <sup>-</sup> ion and Ca <sup>2+</sup> vacancies	[41,42]
		3	551 ± 4	Oxygen vacancies from PO <sub>4</sub> <sup>3-</sup> ion	[41,42]
		i	615 ± 8	Exciton from carbon nanotubes, or OH <sup>-</sup> ion vacancies	[41,42,47]
Second	HAp250-15 HAp250-25 HAp250-35	1	442	Oxygen vacancies from OH <sup>-</sup> ion and OH <sup>-</sup> ion vacancies	[41,42]
		2	499	Oxygen vacancies from OH <sup>-</sup> ion and Ca <sup>2+</sup> vacancies	[41,42]
		3	561	Oxygen vacancies from PO <sub>4</sub> <sup>3-</sup> ion	[41,42]

#### 4. Conclusions

By the co-precipitation method coupled to ultrasonic irradiation, HAp was obtained in the hexagonal phase at 250 and 400 °C without traces of other phases. The morphology of HAp was cylindrical particules, like bars of ~38 nm in length. In the beginning, the application of different thermal treatments to HAp and HAp/OMWCNT composites results in a red shift in the maximum emission of the samples. However, over time, the defects responsible for these shifts were affected by the adsorption/desorption of CO<sub>2</sub>, and their

photoluminescent properties reached an equilibrium point with a blue shift of 54 and 16 nm for the sample HAp400 and the 250 °C composites, respectively. In the case of the sample HAp250, there was a red shift of 13 nm. Even with the addition of different amounts of OMWCNT, the maximum emission of the composites reaches a stabilization value at 250 °C because the OMWCNT are affected by the adsorption/desorption of CO<sub>2</sub>. By deconvolution of the photoluminescence curves, it was found that the defects responsible for the stabilized photoluminescent response in the samples are oxygen vacancies from OH<sup>-</sup> and PO<sub>4</sub><sup>3-</sup> ions and OH<sup>-</sup> and Ca<sup>2+</sup> ion vacancies. This was according to the FTIR results, where the vibrations of OH<sup>-</sup> ions were weak and the substitution of CO<sub>3</sub><sup>2-</sup> for PO<sub>4</sub><sup>3-</sup> and OH<sup>-</sup> ions increased, leading to a higher concentration of vacancies in the samples and to a higher intensity of the photoluminescence response.

Finally, this work has shown that the fabrication of HAp and its composites at 250 °C with small amounts of OMWCNT is suitable to shift and maintain the photoluminescent properties, instead of wasting resources on fabrication at higher temperatures or concentrations of OMWCNT. In this case, the red shift of the photoluminescence emission was achieved without using transition or lanthanide ions. However, this study did not investigate the effect of different amounts of OMWCNT on the mechanical properties of the final composite, which are very important for medical applications. Nevertheless, since different amounts of OMWCNT were investigated, the following studies will be conducted in this way. In this case, as the results show, the OMWCNT amount can be higher, and the maximum emission of the sample over time will remain practically the same. In this way, the most suitable composite for each application can be chosen and further investigated.

**Author Contributions:** Writing—original draft preparation, conceptualization, investigation, data curation, and writing—review and editing, E.X.F.-R.; methodology and writing—review and editing, M.J.R.-Á.; resources, funding acquisition, and writing—review and editing, J.M.-J.; resources, and writing—review and editing, D.H.-C.; writing—review and editing, M.E.R.-G. All authors have read and agreed to the published version of the manuscript.

**Funding:** This research was funded by Consejo Nacional de Ciencia y Tecnología (Conacyt-México), project number INFRA-2015-01-252847 and by the Vicerrectoría de Investigación y Estudios de Posgrado (VIEP) of the Benemérita Universidad Autónoma de Puebla (BUAP), with the projects 100034388-VIEP2019 and 100145955-VIEP2023.

**Institutional Review Board Statement:** Not applicable.

**Informed Consent Statement:** Not applicable.

**Data Availability Statement:** The data presented in this study are openly available in Figueroa Rosales, Edna Xochitl (2023), "FTIR & PL raw data", Mendeley Data, V1, at [<https://doi.org/10.17632/mhk9g942sr.1>].

**Acknowledgments:** E.X.F.-R. wants to thank Conacyt-México for the scholarship (Grant Agreement No. 813372); Instituto de Química from Instituto de Ciencias of the Benemérita Universidad Autónoma de Puebla for the measurements of the FTIR spectra; and Manuel Aguilar Franco of the Laboratorio Nacional de Caracterización de Materiales at Centro de Física Aplicada y Tecnología Avanzada from Universidad Autónoma de México (CFATA-UNAM-México) for the SEM micrographs.

**Conflicts of Interest:** The authors declare no conflict of interest.

## References

1. Castillo-Paz, A.M.; Correa-Piña, B.A.; Martínez-Hernández, H.D.; Gómez-Vázquez, O.M.; Cañon-Davila, D.F.; Zubieta-Otero, L.F.; Londoño-Restrepo, S.M.; Pérez-Torrero, E.; Rodríguez-García, M.E. Influence of the changes in the bone mineral density on the guided bone regeneration using bioinspired grafts: A systematic review and meta-analysis. *Biomed. Mater. Devices* **2022**, *1*–17. [[CrossRef](#)]
2. Ahymah Joshy, M.I.; Elayaraja, K.; Suganthi, R.V.; Chandra Veerla, S.; Kalkura, S.N. In vitro sustained release of amoxicillin from lanthanum hydroxyapatite nano rods. *Curr. Appl. Phys.* **2011**, *11*, 1100–1106. [[CrossRef](#)]
3. Suganthi, R.V.; Elayaraja, K.; Joshy, M.I.A.; Chandra, V.S.; Girija, E.K.; Kalkura, S.N. Fibrous growth of strontium substituted hydroxyapatite and its drug release. *Mater. Sci. Eng. C* **2011**, *31*, 593–599. [[CrossRef](#)]

4. Kolanthai, E.; Ganesan, K.; Epple, M.; Kalkura, S.N. Synthesis of nanosized hydroxyapatite/agarose powders for bone filler and drug delivery application. *Mater. Today Commun.* **2016**, *8*, 31–40. [[CrossRef](#)]
5. Kolanthai, E.; Abinaya Sindu, P.; Thanigai Arul, K.; Sarath Chandra, V.; Manikandan, E.; Narayana Kalkura, S. Agarose encapsulated mesoporous carbonated hydroxyapatite nanocomposites powder for drug delivery. *J. Photochem. Photobiol. B Biol.* **2017**, *166*, 220–231. [[CrossRef](#)] [[PubMed](#)]
6. Hench, L.L. Bioceramics: From concept to clinic. *J. Am. Ceram. Soc.* **1991**, *74*, 1487–1510. [[CrossRef](#)]
7. Constanda, S.; Stan, M.S.; Ciobanu, C.S.; Motelica-Heino, M.; Guégan, R.; Lafdi, K.; Dinischiotu, A.; Predoi, D. Carbon nanotubes-hydroxyapatite nanocomposites for an improved osteoblast cell response. *J. Nanomater.* **2016**, *2016*, 3941501. [[CrossRef](#)]
8. Chen, M.-H.; Yoshioka, T.; Ikoma, T.; Hanagata, N.; Lin, F.-H.; Tanaka, J. Photoluminescence and doping mechanism of theranostic  $\text{Eu}^{3+}/\text{Fe}^{3+}$  dual-doped hydroxyapatite nanoparticles. *Sci. Technol. Adv. Mater.* **2014**, *15*, 055005. [[CrossRef](#)]
9. Mahabole, M.; Bahir, M.; Khairnar, R. Mn blended hydroxyapatite nanoceramic: Bioactivity, dielectric and luminescence studies. *J. Biomimetics Biomater. Tissue Eng.* **2013**, *18*, 43–59. [[CrossRef](#)]
10. Neacsu, I.A.; Stoica, A.E.; Vasile, B.S.; Andronescu, E. Luminescent hydroxyapatite doped with rare earth elements for biomedical applications. *Nanomaterials* **2019**, *9*, 239. [[CrossRef](#)]
11. Paterlini, V.; Bettinelli, M.; Rizzi, R.; El Khouri, A.; Rossi, M.; Della Ventura, G.; Capitelli, F. Characterization and luminescence of  $\text{Eu}^{3+}$ - and  $\text{Gd}^{3+}$ -doped hydroxyapatite  $\text{Ca}_{10}(\text{PO}_4)_6(\text{OH})_2$ . *Crystals* **2020**, *10*, 806. [[CrossRef](#)]
12. Smith, A.M.; Duan, H.; Mohs, A.M.; Nie, S. Bioconjugated quantum dots for in vivo molecular and cellular imaging. *Adv. Drug Deliv. Rev.* **2008**, *60*, 1226–1240. [[CrossRef](#)] [[PubMed](#)]
13. Tite, T.; Popa, A.-C.; Balescu, L.; Bogdan, I.; Pasuk, I.; Ferreira, J.; Stan, G. Cationic Substitutions in Hydroxyapatite: Current Status of the Derived Biofunctional Effects and Their In Vitro Interrogation Methods. *Materials* **2018**, *11*, 2081. [[CrossRef](#)] [[PubMed](#)]
14. Mao, L.-C.; Zhang, X.-Y.; Wei, Y. Recent advances and progress for the fabrication and surface modification of AIE-active organic-inorganic luminescent composites. *Chin. J. Polym. Sci.* **2019**, *37*, 340–351. [[CrossRef](#)]
15. Zakharova, O.V.; Gusev, A.A.; Abourahma, J.; Vorobeva, N.S.; Sokolov, D.V.; Muratov, D.S.; Kuznetsov, D.V.; Sinitskii, A. Nanotoxicity of  $\text{ZrS}_3$  Probed in a Bioluminescence Test on *E. coli* Bacteria: The Effect of Evolving  $\text{H}_2\text{S}$ . *Nanomaterials* **2020**, *10*, 1401. [[CrossRef](#)]
16. Yang, P.; Yang, P.; Teng, X.; Lin, J.; Huang, L. A novel luminescent mesoporous silica/apatite composite for controlled drug release. *J. Mater. Chem.* **2011**, *21*, 5505–5510. [[CrossRef](#)]
17. Chen, F.; Huang, P.; Zhu, Y.-J.; Wu, J.; Zhang, C.-L.; Cui, D.-X. The photoluminescence, drug delivery and imaging properties of multifunctional  $\text{Eu}^{3+}/\text{Gd}^{3+}$  dual-doped hydroxyapatite nanorods. *Biomaterials* **2011**, *32*, 9031–9039. [[CrossRef](#)]
18. Avouris, P.; Chen, J. Nanotube electronics and optoelectronics. *Mater. Today* **2006**, *9*, 46–54. [[CrossRef](#)]
19. Wang, W.; Zhu, Y.; Watari, F.; Liao, S.; Yokoyama, A.; Omori, M.; Ai, H.; Cui, F. Carbon nanotubes/hydroxyapatite nanocomposites fabricated by spark plasma sintering for bonegraft applications. *Appl. Surf. Sci.* **2012**, *262*, 194–199. [[CrossRef](#)]
20. Riggs, J.E.; Guo, Z.; Carroll, D.L.; Sun, Y.-P. Strong luminescence of solubilized carbon nanotubes. *J. Am. Chem. Soc.* **2000**, *122*, 5879–5880. [[CrossRef](#)]
21. O’Connell, M.J. Band gap fluorescence from individual single-walled carbon nanotubes. *Science* **2002**, *297*, 593–596. [[CrossRef](#)] [[PubMed](#)]
22. Zhang, X.; Zhang, J.; Ma, W.; Liao, S.; Zhang, X.; Wang, Z.; Yu, L.; Lian, S. From Nonluminescence to Bright Blue Emission: Boron-Induced Highly Efficient  $\text{Ce}^{3+}$ -Doped Hydroxyapatite Phosphor. *Inorg. Chem.* **2019**, *58*, 13481–13491. [[CrossRef](#)] [[PubMed](#)]
23. Blasse, G.; Grabmaier, B.C. *Luminescent Materials*, 1st ed.; Springer: Berlin/Heidelberg, Germany, 1994; ISBN 978-3-540-58019-5.
24. Machado, T.R.; Sczancoski, J.C.; Beltrán-Mir, H.; Nogueira, I.C.; Li, M.S.; Andrés, J.; Cordoncillo, E.; Longo, E. A novel approach to obtain highly intense self-activated photoluminescence emissions in hydroxyapatite nanoparticles. *J. Solid State Chem.* **2016**, *249*, 64–69. [[CrossRef](#)]
25. Li, J.; Hu, L.; Wang, L.; Zhou, Y.; Grüner, G.; Marks, T.J. Organic Light-Emitting Diodes Having Carbon Nanotube Anodes. *Nano Lett.* **2006**, *6*, 2472–2477. [[CrossRef](#)] [[PubMed](#)]
26. Fournet, P.; Coleman, J.N.; Lahr, B.; Drury, A.; Blau, W.J.; O’Brien, D.F.; Hörhold, H.-H. Enhanced brightness in organic light-emitting diodes using a carbon nanotube composite as an electron-transport layer. *J. Appl. Phys.* **2001**, *90*, 969–975. [[CrossRef](#)]
27. Figueroa-Rosales, E.X.; Martínez-Juárez, J.; García-Díaz, E.; Hernández-Cruz, D.; Sabinas-Hernández, S.A.; Robles-Águila, M.J. Photoluminescent properties of hydroxyapatite and hydroxyapatite/multi-walled carbon nanotube composites. *Crystals* **2021**, *11*, 832. [[CrossRef](#)]
28. Castle, A.B.; Gracia-Espino, E.; Nieto-Delgado, C.; Terrones, H.; Terrones, M.; Hussain, S. Hydroxyl-functionalized and N-doped multiwalled carbon nanotubes decorated with silver nanoparticles preserve cellular function. *ACS Nano* **2011**, *5*, 2458–2466. [[CrossRef](#)]
29. Rabiei, M.; Palevicius, A.; Monshi, A.; Nasiri, S.; Vilkauskas, A.; Janusas, G. Comparing Methods for Calculating Nano Crystal Size of Natural Hydroxyapatite Using X-ray Diffraction. *Nanomaterials* **2020**, *10*, 1627. [[CrossRef](#)]
30. Arul Xavier Stango, S.; Vijayalakshmi, U. Synthesis and characterization of hydroxyapatite/carboxylic acid functionalized MWCNTS composites and its triple layer coatings for biomedical applications. *Ceram. Int.* **2019**, *45*, 69–81. [[CrossRef](#)]
31. Gates-Rector, S.; Blanton, T. The Powder Diffraction File: A quality materials characterization database. *Powder Diffr.* **2019**, *34*, 352–360. [[CrossRef](#)]

32. Vani, R.; Girija, E.K.; Elayaraja, K.; Prakash Parthiban, S.; Kesavamoorthy, R.; Narayana Kalkura, S. Hydrothermal synthesis of porous triphasic hydroxyapatite/ $\alpha$  and  $\beta$  tricalcium phosphate. *J. Mater. Sci. Mater. Med.* **2009**, *20*, 43–48. [[CrossRef](#)] [[PubMed](#)]
33. Londoño-Restrepo, S.M.; Jeronimo-Cruz, R.; Millán-Malo, B.M.; Rivera-Muñoz, E.M.; Rodríguez-García, M.E. Effect of the nano crystal size on the X-ray diffraction patterns of biogenic hydroxyapatite from human, bovine, and porcine bones. *Sci. Rep.* **2019**, *9*, 5915. [[CrossRef](#)] [[PubMed](#)]
34. Yan, L.; Li, Y.; Deng, Z.-X.; Zhuang, J.; Sun, X. Surfactant-assisted hydrothermal synthesis of hydroxyapatite nanorods. *Int. J. Inorg. Mater.* **2001**, *3*, 633–637. [[CrossRef](#)]
35. Dos Santos Silva, D.; Villegas, A.E.C.; Bonfim, R.D.P.F.; Salim, V.M.M.; De Resende, N.S. Iron-substituted hydroxyapatite as a potential photocatalyst for selective reduction of CO<sub>2</sub> with H<sub>2</sub>. *J. CO<sub>2</sub> Util.* **2022**, *63*, 102102. [[CrossRef](#)]
36. Bertinetti, L.; Drouet, C.; Combes, C.; Rey, C.; Tampieri, A.; Coluccia, S.; Martra, G. Surface Characteristics of Nanocrystalline Apatites: Effect of Mg Surface Enrichment on Morphology, Surface Hydration Species, and Cationic Environments. *Langmuir* **2009**, *25*, 5647–5654. [[CrossRef](#)]
37. Hua Cheng, Z.; Yasukawa, A.; Kandori, K.; Ishikawa, T. FTIR study on incorporation of CO<sub>2</sub> into calcium hydroxyapatite. *J. Chem. Soc. Faraday Trans.* **1998**, *94*, 1501–1505. [[CrossRef](#)]
38. Marković, S.; Veselinović, L.; Lukić, M.J.; Karanović, L.; Bračko, I.; Ignjatović, N.; Uskoković, D. Synthetical bone-like and biological hydroxyapatites: A comparative study of crystal structure and morphology. *Biomed. Mater.* **2011**, *6*, 045005. [[CrossRef](#)]
39. Markovic, M.; Fowler, B.O.; Tung, M.S. Preparation and comprehensive characterization of a calcium hydroxyapatite reference material. *J. Res. Natl. Inst. Stand. Technol.* **2004**, *109*, 553–568. [[CrossRef](#)]
40. Zhang, C.; Yang, J.; Quan, Z.; Yang, P.; Li, C.; Hou, Z.; Lin, J. Hydroxyapatite Nano- and Microcrystals with Multiform Morphologies: Controllable Synthesis and Luminescence Properties. *Cryst. Growth Des.* **2009**, *9*, 2725–2733. [[CrossRef](#)]
41. Bystrov, V.S.; Piccirillo, C.; Tobaldi, D.M.; Castro, P.M.L.; Coutinho, J.; Kopyl, S.; Pullar, R.C. Oxygen vacancies, the optical band gap ( $E_g$ ) and photocatalysis of hydroxyapatite: Comparing modelling with measured data. *Appl. Catal. B Environ.* **2016**, *196*, 100–107. [[CrossRef](#)]
42. Huerta, V.J.; Fernández, P.; Gómez, V.; Graeve, O.A.; Herrera, M. Defect-related luminescence properties of hydroxyapatite nanobelts. *Appl. Mater. Today* **2020**, *21*, 100822. [[CrossRef](#)]
43. Bystrov, V.S.; Coutinho, J.; Bystrova, A.V.; Dekhtyar, Y.D.; Pullar, R.C.; Poronin, A.; Palcevskis, E.; Dindune, A.; Alkan, B.; Durucan, C.; et al. Computational study of hydroxyapatite structures, properties and defects. *J. Phys. D: Appl. Phys.* **2015**, *48*, 195302. [[CrossRef](#)]
44. Bystrova, A.V.; Dekhtyar, Y.D.; Popov, A.I.; Bystrov, V.S. Modeling and synchrotron data analysis of modified hydroxyapatite structure. *Math. Biol. Bioinform.* **2014**, *9*, 171–182. [[CrossRef](#)]
45. Sun, W.; Huang, Z.; Zhang, L.; Zhu, J. Luminescence from multi-walled carbon nanotubes and the Eu(III)/multi-walled carbon nanotube composite. *Carbon* **2003**, *41*, 1685–1687. [[CrossRef](#)]
46. Polynskaya, Y.G.; Matsokin, N.A.; Sinita, A.S.; Knizhnik, A.A.; Potapkin, B.V. First-principles investigation of interaction between the atomic oxygen species and carbon nanostructures. *Carbon Trends* **2022**, *9*, 100201. [[CrossRef](#)]
47. Koyama, T.; Miyata, Y.; Asaka, K.; Shinohara, H.; Saito, Y.; Nakamura, A. Ultrafast energy transfer of one-dimensional excitons between carbon nanotubes: A femtosecond time-resolved luminescence study. *Phys. Chem. Chem. Phys.* **2012**, *14*, 1070–1084. [[CrossRef](#)]

**Disclaimer/Publisher’s Note:** The statements, opinions and data contained in all publications are solely those of the individual author(s) and contributor(s) and not of MDPI and/or the editor(s). MDPI and/or the editor(s) disclaim responsibility for any injury to people or property resulting from any ideas, methods, instructions or products referred to in the content.